The DarkLight Experiment:
Searching for the Dark Photon

by

Dustin R. Katzin

Submitted to the Department of Physics
in partial fulfillment of the requirements for the degree of

Bachelor of Science in Physics

at the

MASSACHUSETTS INSTITUTE OF TECHNOLOGY

June 2012

Author . . . .

Department of Physics
May 11, 2012

Certified by . . . . . .

Jesse Thaler
Assistant Professor of Physics
Thesis Supervisor

Accepted by . . . .

Nergis Mavalvala
Professor, Senior Thesis Coordinator, Department of Physics

The DarkLight Experiment:

Searching for the Dark Photon

by

Dustin R. Katzin

Submitted to the Department of Physics
on May 11, 2012, in partial fulfillment of the
requirements for the degree of
Bachelor of Science in Physics

Abstract

We describe a setup to search for the existence of a massive gauge boson A', the "dark photon," mediating dark matter interactions with coupling strength α'. In certain models, the A' decays promptly but invisibly and might be discoverable in high luminosity collider experiments. Following a proposed setup by Wojtsekhowski et al. to use the VEPP-3 electron-positron storage ring at the Budker Institute for Nuclear Physics, we study whether an $e^+ + e^- \to A' + \gamma$ signal could be seen over the quantum electrodynamic background. The proposed VEPP-3 setup is sensitive to an A' within the mass range $m_A = 5-20$ MeV. Out of the two backgrounds, $e^+ + e^- \to 3\gamma$ and $e^+ + e^- \to e^+ + e^- + \gamma$, we find that the former process provides the dominant background for the A' signal. While positron bremsstrahlung events can be detected and suppressed in Wojtsekhowski's apparatus, the 3γ cross-section has a large cross section in this range, "faking" an A'. We use Monte Carlo numerical integration techniques to calculate the cross sections and obtain reach plots, determining which values of $m_{A'}$ and α' could be discovered at 5σ confidence. This background study can be used to improve the VEPP-3 proposal, and provides a valuable comparison study with the MIT-led DarkLight proposal to search for a dark photon in the same mass range.

Thesis Supervisor: Jesse Thaler
Title: Assistant Professor of Physics

Acknowledgments

I am grateful to my thesis advisor Professor Jesse Thaler for his valuable guidance, high expectations, and strong support throughout the research process. I would also like to thank Yonatan Kahn for his feedback and advice.

Contents

Chapter 1

Background and Motivation

Astrophysical measurements have revealed an anomalous matter distribution through-out the universe, which cannot be explained by the gravitational interactions of visible matter. Measurements from galactic rotational curves to cosmic microwave back-ground observation [1] indicate the existence of dark matter, a mysterious entity that interacts with gravity but not electromagnetism. Because gravity is the weakest known fundamental force, dark matter is difficult to test with terrestrial experiments, and precision measurements are needed to determine whether dark matter has non-gravitational interactions with ordinary matter. The eventual goal is to discern the nature of dark matter, and whether or not we can describe it within current particle paradigms, such as the neutralinos predicted by supersymmetry [2].

Except for the absence of dark matter, the Standard Model, encompassing the physics of quarks, leptons, the Higgs boson, and the gauge bosons, is a successful physical theory of fundamental interactions. It has passed many experimental tests. For example, the quantum electrodynamic fine-structure constant has been measured precisely from numerous experiments, including the Lamb shift, hyperfine splitting, quantum Hall effect, and AC Josephson effect [3]. Because of this, QED provides a tool for accurately probing the structure of elementary particles. Surprisingly, we will show in this thesis that precision tests of QED may be able to probe aspects of dark matter.

An intriguing paradigm for dark matter is that it might interact via a "dark

force." [4, 5]. A new light force-carrying boson, called an A' boson, or dark photon, would mediate the dark force. One model consists of a $g\bar{\psi}A'\psi$ interaction, quantum electrodynamics with a massive photon, with coupling constant g to be determined experimentally. Throughout this thesis, we refer to $\alpha' = \dfrac{g^2}{4\pi}$ as the coupling constant of the theory. This interaction allows the process $e^+ + e^- \to \gamma A'$ to occur. Recent astrophysical anomalies give tantalizing hints towards this proposal, such as a high fraction of positrons among cosmic ray particles, found by the PAMELA satellite [6]. Based on data collected between July 2006 and February 2008, these results showed a significant increase in positron fraction with energy [6]. This is inconsistent with our current knowledge of cosmic rays; an additional mechanism for positron production is necessary. Dark matter pair annihilation is the proposed conversion of a dark matter particle and an anti-dark matter particle into two dark photons, which can then decay to electron-positron pairs via $A' \to e^+ e^-$. This is a candidate for the additional positron source. In addition, the Standard Model prediction for the anomalous $g - 2$ of the muon differs from observation by 3.6σ [7]. An additional gauge boson with mass between 10-100 MeV may resolve this discrepancy.

Within the same dark force paradigm, the A' might decay invisibly, either to dark matter itself or to neutrinos [8]. Wojtsekhowski et al. proposed [9] an invisible A' search, in which the A' is produced but its decay products are not detected, using the VEPP-3 electron-positron storage ring situated at the Budker Institute for Nuclear Physics. In their proposal, a 500 MeV beam of positrons is incident on an electron target, and a segmented photometer may detect one or two outgoing photons. If only one is detected, it may have originated from the process $e^+ e^- \to \gamma A'$. Wojtsekhowski et al. compare this signal with $e^+ e^- \to 2\gamma$ and positron bremsstrahlung $e^+ e^- \to e^+ e^- \gamma$ backgrounds. We will explain why the 2γ process is not a background for the A' signal process, and present a careful treatment of an $e^+ e^- \to 3\gamma$ background. If the $e^+ e^- \to e^+ e^- \gamma$ background is suppressed, then $e^+ e^- \to 3\gamma$ is the dominant background.

In this thesis, we study the production of dark photons by $e^+ e^- \to \gamma A'$, and determine the experimental reach for the Wojtsekhowski et al. proposal. A reach

plot [10] shows the region in the (m'_A, α') plane where a dark photon could be discovered above the QED background. A narrow resonance in the reconstructed A' invariant mass spectrum would support the existence of a dark photon which interacts with known particles by our proposed interaction. As we will show, even though the A' cannot be detected directly, the photon kinematics is sufficient to determine the A' mass.

By studying the VEPP-3 experiment, we can gain valuable information for an MIT-led proposal [11] called DarkLight (for Detecting A Resonance Kinematically with eLectrons Incident on a Gaseous Hydrogen Target). The DarkLight apparatus would be situated at Jefferson Lab (JLab), and would be included in the Free Electron Laser (FEL) in 2014-2015. Test data is being collected in 2012. The DarkLight apparatus will collide the JLab FEL 100 MeV electron beam with a stationary hydrogen target, and search for a narrow resonance in the reconstructed $e^+ e^-$ invariant mass spectrum [11]. This resonance would be the signature of the dark photon proposed for cosmic-ray positron production: dark-matter pair-annihilates to the A', which then decays to an electron-positron pair. Studies are ongoing as to whether DarkLight could be sensitive to an invisible A' decay, since DarkLight is not currently optimized for such a search. DarkLight, though it uses Rutherford scattering rather than $e^+ e^-$ annihilation, could in principle control QED backgrounds by detecting all final-state particles. This work motivates the incorporation of invisible A' search into the DarkLight apparatus.

The remainder of this thesis is organized as follows. In Chapter 2, we discuss the experimental proposal [9] by Wojtsekhowski et al. In Chapter 3, we present our Monte Carlo phase-space integration technique, and give a few easily verifiable test cases. In Chapter 4, we compute the matrix elements of the signal and background processes. The signal matrix element is a straightforward calculation given in Appendix B. The background matrix elements are significantly more difficult to calculate, but we were able to obtain numerical matrix elements using MadGraph 5 [12], as discussed in Chapter 5. In Chapter 6, we present the reach of the VEPP-3 proposal and cross section histograms for each background process. We conclude in Chapter 7 by

discussing the relevance of this study for DarkLight.

Chapter 2

Experimental Setup

2.1   Signal and Background Processes

We perform an analysis of the experimental setup proposed by Nikolenko, Rachek, and Wojtsekhowski in [9], determining the 5σ confidence potential discovery range for the existence of the A'. This setup is capable of detecting the A' in the mass range $5 - 20$ MeV. The experiment proposed in [9] was designed for the VEPP-3 electron-positron storage ring at the Budker Institute for Nuclear Physics.

Wojtsekhowski et al. proposed an experimental search shown in Figure 2-1 [9] over the dominant pair-annihilation background. The apparatus contains a segmented photon detector between $1.5°$ and $4.5°$, which is sensitive to the signal process $e^+\, e^- \rightarrow \gamma\, A'$. Wojtsekhowski's setup includes partial measures for separating the signal from the QED background. If both detectors register a photon, then the process is $e^+\, e^- \rightarrow 2\gamma + X$, where X denotes zero or more additional outgoing particles, and the event is thrown out. This eliminates the large $e^+\, e^- \rightarrow 2\gamma$ background, which is the dominant QED process. If only one detector registers, then the event may have either two or three outgoing particles. If there are two outgoing particles, the photon originated from the signal process. In addition, the setup is surrounded by a positron veto, which detects outgoing positrons with a $\dfrac{1}{50}$ failure rate [9]. If the veto detects a positron, then the event is thrown out. The signal process cannot be completely separated from the background by the VEPP-3 apparatus.
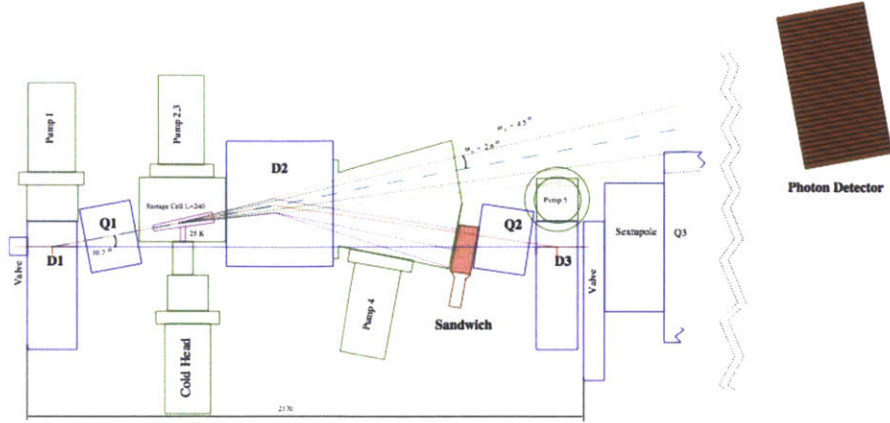
13

Figure 2-1: The interior of the setup proposed by Wojtsekhowski. The photometer spans the angular range 1.5° to 4.5°. A positron veto is downstream of the D_2 detector.

The leading order background processes are

(BG1) $e^+ e^- \to \gamma \gamma \gamma$ and

(BG2) $e^+ e^- \to \gamma e^+ e^-$.

Feynman diagrams for the signal and background processes are displayed in Figures 2-2, 2-3. We also give the lab frame kinematics in Figures 2-4, 2-5, and 2-6.

We must include both backgrounds in an analysis of Wojtsekhowski's setup. If just one photon is detected, it is possible that there are two other photons in the final state with a nonzero composite invariant mass, faking an A'. It is impossible to distinguish a single event of this type (BG1) from a signal event without additional photon detectors. In principle, if the setup contained an ideal positron veto, all (BG2) processes could be identified and eliminated. The positron veto at VEPP-3 suppresses the (BG2) background, but does not eliminate it entirely due to the $\frac{1}{50}$ failure rate.

The occurrences of a given background event are Poisson distributed with fluctuations $\sim \frac{1}{\sqrt{\mathcal{N}}}$, where $\mathcal{N}$ is the number of events. For each event, the detector either accepts it as a possible signal or throws it out. If the number of possible signals exceeds the expectation value of the Poisson distribution by more than $5\sigma = 5\sqrt{\mathcal{N}}$, then we say with higher than 5σ confidence that the A' exists. This information is visualized in a reach plot, showing the smallest 5σ-detectable coupling constant for a
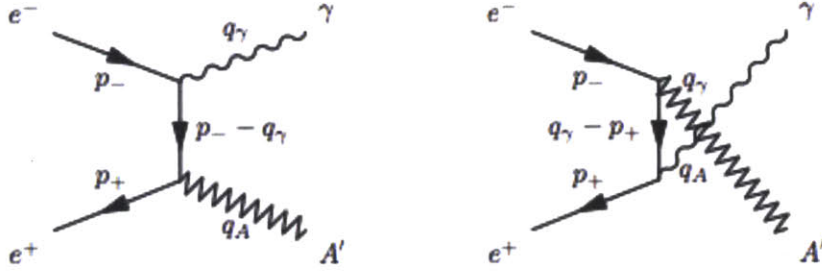
14

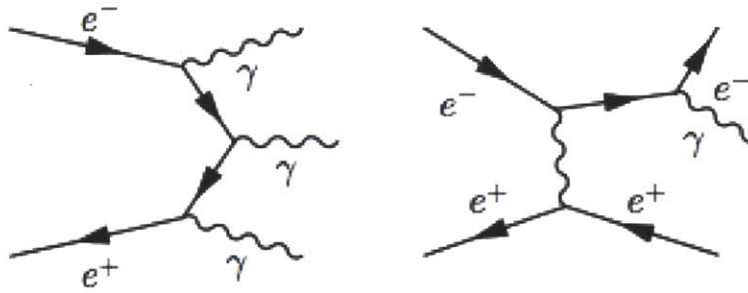Figure 2-2: Feynman diagrams for the signal process (S) $e^+ e^- \to \gamma A'$.

Figure 2-3: Feynman diagrams for the background processes (BG1) $e^+ e^- \to 3\gamma$ and (BG2) $e^+ e^- \to e^+ e^- \gamma$, respectively. For clarity, we do not show the crossed diagrams.

given A' mass.

It is useful to contrast this signal and background with that of the DarkLight apparatus. DarkLight would produce A' as a product of Rutherford scattering, with signal $e\, p \to e\, p\, A'$ and dominant background for invisible A' decays $e\, p \to e\, p\, \gamma\, \gamma$. For DarkLight, both the signal and background would have more particles in the final state than the analogous processes for Wojtsekhowski's setup, so the cross sections are necessarily smaller. For each additional final-state particle, there is an extra phase space normalization factor that decreases the total cross section. However, DarkLight would have a larger signal-to-background cross section ratio, since it could detect and identify all final-state particles, improving the signal separation. The reach of both setups should be comparable.
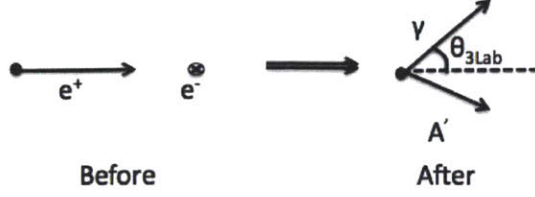
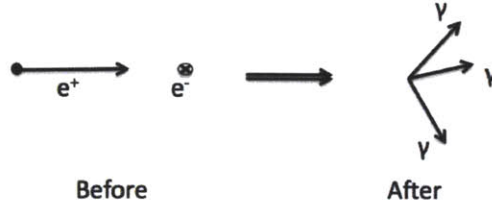Figure 2-4: Kinematics for the signal process, $e^+ e^- \to \gamma A'$, in the lab frame.

Figure 2-5: Kinematics for the background process $e^+ e^- \to 3\gamma$ in the lab frame.

2.2 Detector Constraints

We enumerate the particles from 1 to 5, such that particle 3 is a photon in both processes. The invariant mass of particles 4 and 5, m_{45}, is nonzero, and acts as a fictitious A'. If a real A' is observed, a signal A' cross section from the (S) process must occur above the fictitious A' background. [9] proposed that the (BG2) process alone constitutes the dominant background for the signal. We will see that this background is manageable for invariant masses in the suspected range of the A', $m_{A'} = 5 - 20$ MeV. However, since the (BG2) process is suppressed by the positron veto, the (BG1) process is much larger, providing the dominant background for the A' in its mass range. For the dominant background of the signal process over the full invariant mass range, we must overlay (BG1) and (BG2), obtaining a composite background.

Let E_{3Lab} and θ_{3Lab} denote the lab frame energy and scattering angle of one of the photons in the final state of the scattering process. The photons are indistinguishable, so it does not matter which we choose. But we must account for multiple counting by
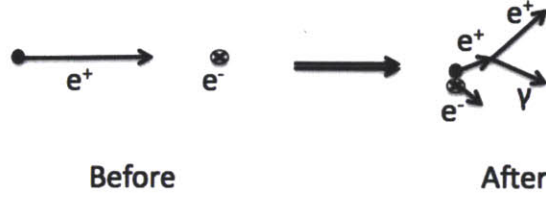
Before   **After**

Figure 2-6: Kinematics for the background process $e^+ e^- \to e^+ e^- \gamma$ in the lab frame.

restricting to a $\frac{1}{3!}$ fraction of phase space. Following [9], we restrict to photon energies E_{3Lab} between 50 and 400 MeV, and scattering angle θ_{3Lab} between $1.5°$ and $4.5°$, the range of the detector, in both processes. We take the beam energy to be $E_{beam} = 500$ MeV, and the instantaneous luminosity to be 10^{32} cm^{-2}s^{-1} = 10^{-4} pbarn s^{-1}. Over 6 months at 75% efficiency, the integrated luminosity is 1166.4 pbarn. For (BG1), there is a soft photon singularity in the limit that one of the photon energies gets small. We regulate this singularity by imposing a lower bound of 1 MeV on E_{4Lab} and E_{5Lab}, the other two photon energies. We also ensure that only one of the photons is observed in the given angular range; θ_{4Lab} and θ_{5Lab} must both be outside this range, so that exactly one photon impinges on the detector. For (BG2), we restrict to E_{3Lab} between 50 and 400 MeV, and scattering angles $\theta_{3Lab}, \theta_{4Lab}$ between $1.5°$ and $4.5°$, so that the photon and positron are both detected. Here the label 3 refers to the photon, 4 to the positron, and 5 to the electron.

In both background processes, we detect a photon and treat the other two outgoing particles as a composite particle. The constraints we have imposed on the background mimic the constraints on the signal process, treating the background composite particle as we treat the A' in the signal. We do this because, for the signal process, the photon is the only detectable outgoing particle. Since $e^+ + e^- \to \gamma A'$ is a $2 \to 2$ scattering, the A' momentum q_A can be entirely reconstructed from the measured momentum q_γ of the photon.

In [9], the following detector resolutions are given: $\frac{\sigma_E}{E} = 5\%$ for the energy of a photon, and $\sigma_\theta = 0.1°$ for the angle off of the scattering axis. For the reach plots, we will see that it suffices to compute the resolution of m_{45}, the invariant composite mass

17

of two outgoing particles that are not photons, for the $2 \to 3$ background processes. We compute m_{45} in terms of the center-of-mass energy E_{CM}, which is easily related to E_{beam} by a simple Lorentz transformation: see the calculation in Chapter 4 for details. There, we show that

$$E_{CM} = \sqrt{2m(E_{beam} + m)}, \tag{2.1}$$

where m is the electron mass. For p_1 and p_2 the incoming momenta, and p_3 the momentum of an outgoing photon, we have in the center-of-mass frame (with E_3 now the energy of the outgoing photon in the CM frame):

$$m_{45}^2 = (p_1 + p_2 - p_3)^2 = (E_{CM} - E_3)^2 - \vec{p}_3^2 = E_{CM}^2 - 2E_3 E_{CM}. \tag{2.2}$$

So $m_{45} = \sqrt{E_{CM}^2 - 2\gamma(1 - \beta)E_{3Lab}E_{CM}}$, where $\gamma = \dfrac{E_{CM}}{2m} = (1 - \beta^2)^{-\frac{1}{2}}$. Using standard error-propagation techniques described in [13], we find the resolution on m_{45} to be

$$
\begin{aligned}
\sigma_{m_{45}} &= \left(\frac{\partial \sqrt{E_{CM}^2 - 2\gamma(1 - \beta)E_{3Lab}E_{CM}}}{\partial E_{3Lab}} \cdot 0.05 E_{3Lab} \right) \\
&= 0.05 \frac{E_{CM} E_{3Lab} \gamma(1 - \beta)}{\sqrt{E_{CM}^2 - 2\gamma(1 - \beta)E_3 E_{CM}}} \\
&= 0.05 \frac{E_{CM} E_3}{m_{45}}. \tag{2.3}
\end{aligned}
$$

In terms of E_{CM} and m_{45} alone, we have

$$\sigma_{m_{45}} = 0.05 \times \frac{E_{CM}^2 - m_{45}^2}{2m_{45}}. \tag{2.4}$$

Since m_{45} is a function of E_3, independent of θ_3, the angular resolution σ_θ does not affect the mass resolution $\sigma_{m_{45}}$. The mass resolution is plotted in Figure 2-7.
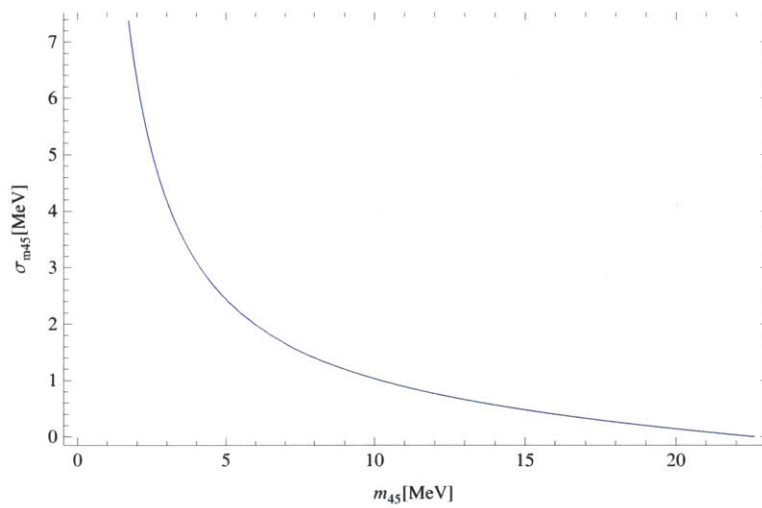
18

Figure 2-7: Plot of the mass resolution $\sigma_{m_{45}}$ as a function of the composite invariant mass m_{45}.

Chapter 3

Monte Carlo Techniques for

Phase-Space Integration

The differential cross section of a scattering process $p_1 + p_2 \to p_3 + \cdots + p_n$ is given by eq. (6.38) in [14].

$$
\begin{aligned}
d\sigma &= \frac{S}{4\sqrt{(p_1 \cdot p_2)^2 - (m_1 m_2)^2}} |\mathcal{M}|^2 (2\pi)^4 \delta^{(4)}(p_1 + p_2 - p_3 - \cdots - p_n) \\
&\times \prod_{j=3}^{n} \frac{1}{2\sqrt{\vec{p}_j^2 + m_j^2}} \frac{d^3 \vec{p}_j}{(2\pi)^3},
\end{aligned} \tag{3.1}
$$

where S is the symmetry factor due to identical particles in the final state, and $\mathcal{M}$ is the matrix element. We obtain the total cross sections for the signal and background processes by calculating the matrix element and then performing the phase space integration, with the lab cuts imposed by additional Heaviside theta factors included in the differential cross section.

The matrix element for the signal process was computed analytically. However, for the $2 \to 3$ background processes, we computed matrix elements numerically using MadGraph 5 [12]. MadGraph, developed by the University of Illinois: Urbana-Champaign, is Fortran-based software which can numerically generate a matrix element, given all of the kinematic information for a scattering event. It is typically used for processes involving Standard Model particles, such as the two background

21

processes. MadGraph assumes the high-energy limit, eliminating the electron mass, but we will later discuss a work-around to put this mass back in the calculation.

In general, the $2 \to 3$ phase space integrals are too difficult to do by hand, so we evaluated them numerically by the Monte Carlo algorithm [15]. Monte Carlo integration takes as input a weight function $w(x_1, \cdots, x_{N_x})$, where N_x is the number of parameters, and returns the approximate integral of w over the rectangle $[a_1, b_1] \times \cdots \times [a_{N_x}, b_{N_x}]$. From the definition of the average value $\langle w \rangle$,

$$\int_{a_1}^{b_1} \cdots \int_{a_{N_x}}^{b_{N_x}} dx_1 \cdots dx_{N_x} \, w(x_1, \cdots, x_{N_x}) = \left(\prod_{j=1}^{N_x} (b_j - a_j) \right) \langle w \rangle. \qquad (3.2)$$

The Monte Carlo technique is to randomly generate events, sets of values for the x_j, and evaluate w on each set to obtain a sequence of values w_i, $i = 1, \cdots, \mathcal{N}$, where $\mathcal{N}$ is the number of events. Then we simply have

$$\langle w \rangle = \frac{1}{\mathcal{N}} \sum_{i=1}^{\mathcal{N}} w_i, \qquad (3.3)$$

and by comparison,

$$\int_{a_1}^{b_1} \cdots \int_{a_{N_x}}^{b_{N_x}} dx_1 \cdots dx_{N_x} \, w(x_1, \cdots, x_{N_x}) = \frac{1}{\mathcal{N}} \left(\prod_{j=1}^{N_x} (b_j - a_j) \right) \sum_{i=1}^{\mathcal{N}} w_i. \qquad (3.4)$$

To obtain reach plots, we need to integrate the differential cross section over Lorentz-invariant phase-space. We will specialize this general Monte Carlo integration prescription to this task. First, we give an analytic tool for unifying the phase space integration for both background processes.

In each process, all of the momenta are determined by a small set of center-of-mass parameters. For the signal process, we use the scattering angle θ_{CM}, defined as the angle $\vec{p}_3$ makes with $\vec{p}_1$ in the CM frame. For the $2 \to 3$ processes, we used a cascaded $2 \to 2$ scheme, for which $p_1 + p_2 \to p_3 + p_Q$, and then $p_Q \to p_4 + p_5$. p_Q is a composite state with an undetermined invariant mass, which we integrate over. We think of $p_1 + p_2 = p_{CM}$ as a decaying composite rest particle. The full analysis is

contained in Appendix A, and we give the result here:

$$\int d\Phi_3 = \frac{1}{(2\pi)(32\pi^2)^2} \int_{(m_2+m_3)^2}^{(E_{cm}-m_1)^2} dQ^2 \left[\sqrt{c_1^4 + c_q^4 + 1 - 2c_1^2 c_q^2 - 2c_1^2 - 2c_q^2} \right.$$

$$\left. \times \sqrt{\left(\frac{c_2}{c_q}\right)^4 + \left(\frac{c_3}{c_q}\right)^4 + 1 - 2\left(\frac{c_2}{c_q} \cdot \frac{c_3}{c_q}\right)^2 - 2\left(\frac{c_2}{c_q}\right)^2 - 2\left(\frac{c_3}{c_q}\right)^2} \right]$$

$$\times d\Omega_{1q} d\Omega_{23},$$

$$(3.5)$$

where Q is the fictitious mass of the outgoing composite of particles 4 and 5, and $c_q = \frac{Q}{E_{cm}}$, $c_i = \frac{m_i}{E_{cm}}$, $i = 1, 2, 3$.

The main advantage to using cascaded $2 \rightarrow 2$ for the background processes is that all $2 \rightarrow 3$ phase space integrals may be treated identically: just set up the integrand as a product of $2 \rightarrow 2$ phase space integrals, and use c_q^2, θ_{1q}, ϕ_{1q}, θ_{23}, and ϕ_{23} as the five center-of-mass parameters. Note that the Jacobian between solid angles is 1, since the change-of-variables matrix is in $SO(3)$. So we can use any two independent solid angles. It is most convenient to use the solid angles for the directions of p_3 and p_4.

Once the N_x independent center-of-mass parameters have been chosen, we randomly generate a table of sets of values for these parameters, and evaluate the differential cross section at each value. Each center-of-mass parameter x_j is uniformly generated over an interval $[a_j, b_j]$, with length $l_j = b_j - a_j$, $j = 1, \cdots N_x$. Denote the parameter volume by $V_x = \prod_{j=1}^{N_x} l_j$. Let $d\sigma_i$ denote these values, indexed by $i = 1, \cdots, \mathcal{N}$, with $\mathcal{N}$ the total number of events. Then we define the total cross section σ and uncertainty $\Delta\sigma$ by

$$\sigma = \frac{V_x}{\mathcal{N}} \left(\sum_{i=1}^{\mathcal{N}} d\sigma_i \right), \qquad (3.6)$$

$$\Delta\sigma = \left[\frac{1}{\mathcal{N}} \left(\sum_{i=1}^{\mathcal{N}} (V_x d\sigma_i - \sigma)^2 \right) \right]^{\frac{1}{2}}. \qquad (3.7)$$

23

We generate histograms of the differential cross section over any function $f(x_1, \cdots, x_{N_x})$ of the CM parameters over an interval $[f_{min}, f_{max}]$, by partitioning this interval into bins $I_k = [f_{k-1}, f_k]$, $k = 1, \cdots, N_{bins}$. Here N_{bins} is the number of bins, and $f_0 = f_{min}$, $f_{N_{bins}} = f_{max}$.

Define $d\sigma_{ik}$ to be $d\sigma_i$ if the set of center-of-mass parameters, $\{x_j\}$, that yielded the differential cross section $d\sigma_i$ satisfies $f(x_1, \cdots, x_{N_x}) \in I_k$, and set $d\sigma_{ik}$ to be 0 otherwise. We give $\dfrac{d\sigma}{df}$ as a histogram over the bin partition $\{I_k\}$, by setting

$$\frac{d\sigma}{df}(I_k) \;=\; \frac{V_x}{\mathcal{N}(f_k - f_{k-1})}\left(\sum_{i=1}^{\mathcal{N}} d\sigma_{ik}\right), \tag{3.8}$$

$$\Delta\frac{d\sigma}{df}(I_k) \;=\; \left[\frac{1}{\mathcal{N}(f_k - f_{k-1})}\sum_{i=1}^{\mathcal{N}}\left(V_x d\sigma_{ik} - \frac{d\sigma}{df}(I_k)\right)^2\right]^{\frac{1}{2}}. \tag{3.9}$$

We check that if we integrate over f, we get back the total cross section:

$$\begin{aligned}
\int_{f_{min}}^{f_{max}} \frac{d\sigma}{df}df \;&=\; \sum_{k=1}^{N_{bins}} \frac{d\sigma}{df}(I_k) \cdot (f_k - f_{k-1}) \\
&=\; \frac{1}{\mathcal{N}} \sum_{k=1}^{N_{bins}} \left(\sum_{i=1}^{\mathcal{N}} d\sigma_{ik}\right)\left(\prod_{j=1}^{N_x} l_j\right) \\
&=\; \frac{1}{\mathcal{N}}\left(\sum_{i=1}^{\mathcal{N}} d\sigma_i\right)\left(\prod_{j=1}^{N_x} l_j\right) \\
&=\; \sigma. \tag{3.10}
\end{aligned}$$

Note that since all of the $d\sigma_i$ values are nonzero for exactly one value of k, we have the relation $\displaystyle\sum_{k=1}^{N_{bins}} d\sigma_{ik} = d\sigma_i$.

3.1 Monte Carlo: Basic Test Cases

To see that the method works, we begin with the simplest possible weight function, $w(\theta) \equiv 1$. Here, the parameter θ is sampled uniformly from the interval $[0, 2\pi]$. Upon applying the Monte Carlo method, we find the total cross section $\sigma = 6.283 \pm$
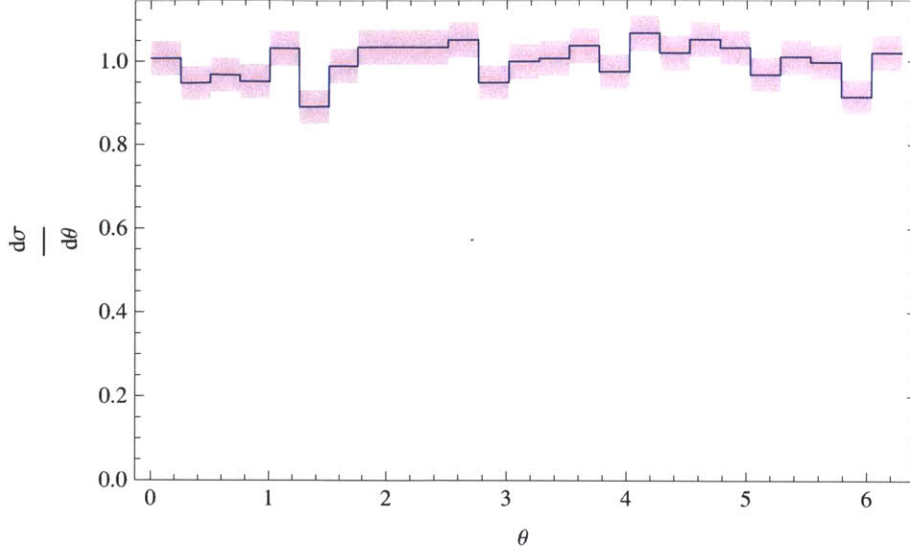
Figure 3-1: Histogram over $f(\theta) = \theta$ for the trivial weight $w(\theta) = 1$. The blue curve is the differential cross section $\dfrac{d\sigma}{df}$, and the pink shaded region is the uncertainty.

(1.2×10^{-12}), as expected. In Figure 3-1, we present a histogram over the function $f(\theta) = \theta$, with $\mathcal{N} = 10000$ events and $N_{bins} = 25$ bins. For every histogram in this paper, the blue curve is $\dfrac{d\sigma}{df}$, and the pink shaded region encompasses the region $\left[\dfrac{d\sigma}{df} - \Delta\dfrac{d\sigma}{df}, \dfrac{d\sigma}{df} + \Delta\dfrac{d\sigma}{df}\right]$. We expect the uncertainty to vary with the number of events $\mathcal{N}$ as $\mathcal{O}(\mathcal{N}^{-\frac{1}{2}})$. That is, for $\mathcal{N} = 10000$, the uncertainty should be on the order of 10^{-2}. We see from the figure that this is the case, as the uncertainty is about 0.05.

We performed a similar calculation with the weight function $w(\theta) = \sin\theta$, with θ sampled from $[0, \pi]$. The total cross section should give us $\int_0^\pi \sin\theta d\theta = 2$. The Monte Carlo result for $\mathcal{N} = 10000$ is $\sigma = 1.999 \pm 0.966743$. With $N_{bins} = 25$, we obtain the histogram in Figure 3-2. This histogram clearly traces out $\sin\theta$ for $\theta \in [0, \pi]$, as expected.
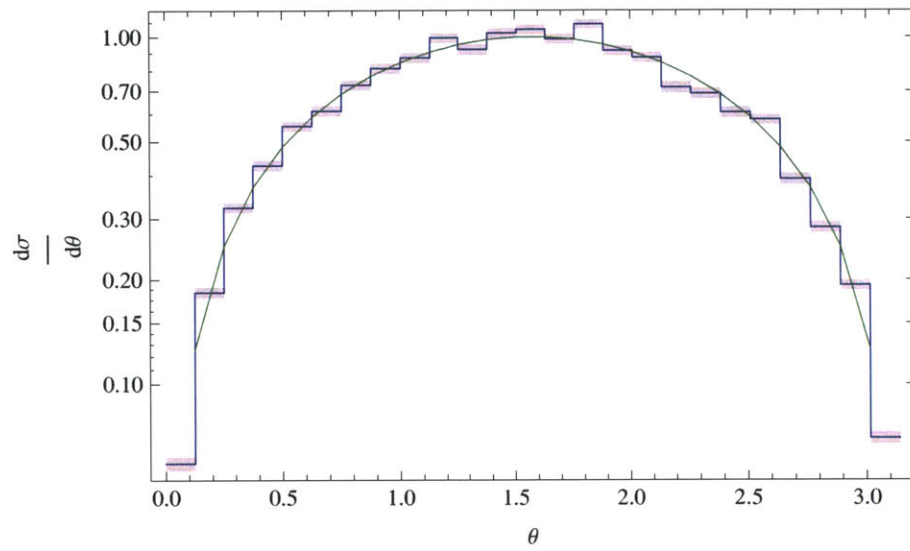
Figure 3-2: Histogram over $f(\theta) = \theta$ for the weight $w(\theta) = \sin\theta$. The green curve is a plot of $\sin\theta$ for comparison.

Chapter 4

Computation of the Matrix Elements

4.1 Signal Cross Section & Kinematics

The signal cross section is computed analytically in Appendix B. The matrix element is

$$\overline{|\mathcal{M}|^2} = \frac{g^2 e^2}{4} \left[\frac{\text{I}}{4(p_- \cdot q_\gamma)^2} - \frac{\text{II}}{2(p_- \cdot q_\gamma)(p_+ \cdot q_\gamma)} + \frac{\text{IV}}{4(p_+ \cdot q_\gamma)^2} \right], \tag{4.1}$$

where

$$\text{I} = 8[tu - m^2(2s + 5t + 3u) + 3m^4], \tag{4.2}$$

$$\text{II} = 8[-M^2 s + m^2(M^2 - s) + 2m^4] \tag{4.3}$$

$$\text{IV} = 8[tu - m^2(2s + 5u + 3t) + 3m^4], \tag{4.4}$$

given in terms of electron mass m, the A' mass M, and the Mandlestam variables s, t, u. The resulting cross section is given in Appendix B as

$$\frac{d\sigma}{d\theta_{CM}} = \frac{1}{32\pi E_{CM}^2} \cdot \frac{E_\gamma}{|\vec{p}_+|} \overline{|\mathcal{M}|^2}, \tag{4.5}$$

where $E_\gamma = \dfrac{E_{CM}^2 - M^2}{2E_{CM}}$.

We give the kinematics here, computing the Lorentz transformation below:

The lab frame is defined by $p_- = (m, 0, 0, 0)$, $p_+ = (E_{beam}, -\sqrt{E_{beam}^2 - m^2}, 0, 0)$. E_{beam} is the positron beam energy, fixed by the experimental setup: $E_{beam} = 500$ MeV. The transformation between the lab and CM frames is given by the as-yet undetermined Lorentz transformation

$$\begin{pmatrix} m \\ 0 \end{pmatrix} = \begin{pmatrix} \gamma & \beta\gamma \\ \beta\gamma & \gamma \end{pmatrix} \begin{pmatrix} E_{CM}/2 \\ \sqrt{(E_{CM}/2)^2 - m^2} \end{pmatrix}. \tag{4.6}$$

So $\gamma(\frac{E_{CM}}{2} + \beta\sqrt{(\frac{E_{CM}}{2})^2 - m^2}) = m$ and $\beta\frac{E_{CM}}{2} + \sqrt{(\frac{E_{CM}}{2})^2 - m^2} = 0$, and we obtain $\beta = -\sqrt{1 - \frac{4m^2}{E_{CM}^2}}$.

We have $\gamma(\frac{E_{CM}}{2} - \frac{2}{E_{CM}}((\frac{E_{CM}}{2})^2 - m^2)) = m$, so that $\gamma = \dfrac{E_{CM}}{2m}$. We now determine E_{CM} as a function of E_{beam}.

$$\begin{pmatrix} E_{beam} \\ -\sqrt{E_{beam}^2 - m^2} \end{pmatrix} = \begin{pmatrix} \gamma & \beta\gamma \\ \beta\gamma & \gamma \end{pmatrix} \begin{pmatrix} E_{CM}/2 \\ -\sqrt{(E_{CM}/2)^2 - m^2} \end{pmatrix}. \tag{4.7}$$

This gives

$$E_{beam} = \gamma(\frac{E_{CM}}{2} + \beta\sqrt{(\frac{E_{CM}}{2})^2 - m^2}) = \gamma(\frac{E_{CM}}{2} + \frac{2}{E_{CM}}((\frac{E_{CM}}{2})^2 - m^2)) = \gamma E_{CM} - m, \tag{4.8}$$

so that

$$E_{beam} = \frac{E_{CM}^2}{2m} - m, \tag{4.9}$$

$$E_{CM} = \sqrt{2m(E_{beam} + m)} = 22.6 \text{ MeV}. \tag{4.10}$$

The kinematics require that $M < E_{CM}$, giving an upper bound on the A' mass of $M < 22.6$ MeV. For completeness, we give the lab variables θ_γ^{Lab}, E_γ^{Lab}, θ_A^{Lab}, and

28

E_A^{Lab} as functions of the CM variables:

$$q_\gamma^{Lab} = \begin{pmatrix} \gamma & 0 & 0 & \beta\gamma \\ 0 & 1 & 0 & 0 \\ 0 & 0 & 1 & 0 \\ \beta\gamma & 0 & 0 & \gamma \end{pmatrix} \begin{pmatrix} E_\gamma \\ E_\gamma \sin\theta_{CM} \\ 0 \\ E_\gamma \cos\theta_{CM} \end{pmatrix} = \begin{pmatrix} \gamma E_\gamma(1 + \beta\cos\theta_{CM}) \\ E_\gamma \sin\theta_{CM} \\ 0 \\ \gamma E_\gamma(\beta + \cos\theta_{CM}) \end{pmatrix}. \qquad (4.11)$$

So

$$E_\gamma^{Lab} = \gamma E_\gamma(1 + \beta\cos\theta_{CM}), \qquad (4.12)$$

$$\theta_\gamma^{Lab} = \tan^{-1}\frac{\sin\theta_{CM}}{\gamma(\beta + \cos\theta_{CM})}. \qquad (4.13)$$

Similarly,

$$q_A^{Lab} = \begin{pmatrix} \gamma & 0 & 0 & \beta\gamma \\ 0 & 1 & 0 & 0 \\ 0 & 0 & 1 & 0 \\ \beta\gamma & 0 & 0 & \gamma \end{pmatrix} \begin{pmatrix} E_{CM} - E_\gamma \\ -E_\gamma \sin\theta_{CM} \\ 0 \\ -E_\gamma \cos\theta_{CM} \end{pmatrix} = \begin{pmatrix} \gamma[E_{CM} - E_\gamma(1 + \beta\cos\theta_{CM})] \\ -E_\gamma \sin\theta_{CM} \\ 0 \\ \gamma[\beta E_{CM} - E_\gamma(\beta + \cos\theta_{CM})] \end{pmatrix},$$

$$(4.14)$$

and we have

$$E_A^{Lab} = \gamma[E_{CM} - E_\gamma(1 + \beta\cos\theta_{CM})], \qquad (4.15)$$

$$\theta_\gamma^{Lab} = \tan^{-1}\frac{-E_\gamma \sin\theta_{CM}}{\gamma[\beta E_{CM} - E_\gamma(\beta + \cos\theta_{CM})]}. \qquad (4.16)$$

We present a Monte Carlo computation of the total unconstrained signal cross section as a function of the A' mass in Figure 4-1. Note that the total cross section σ grows as a function of the A' mass M, and the matrix element appears to become formally infinite at $M = E_{CM}$, where $E_\gamma = 0$. This results from the infrared singularity of the soft-photon limit in quantum electrodynamics [3]. This divergence is cancelled by a loop diagram, so that the matrix element is finite at $M = E_{CM}$. Then the factor of E_γ in the phase space causes the differential cross section to vanish, and so the total cross section also vanishes as expected. But this is unphysical: when
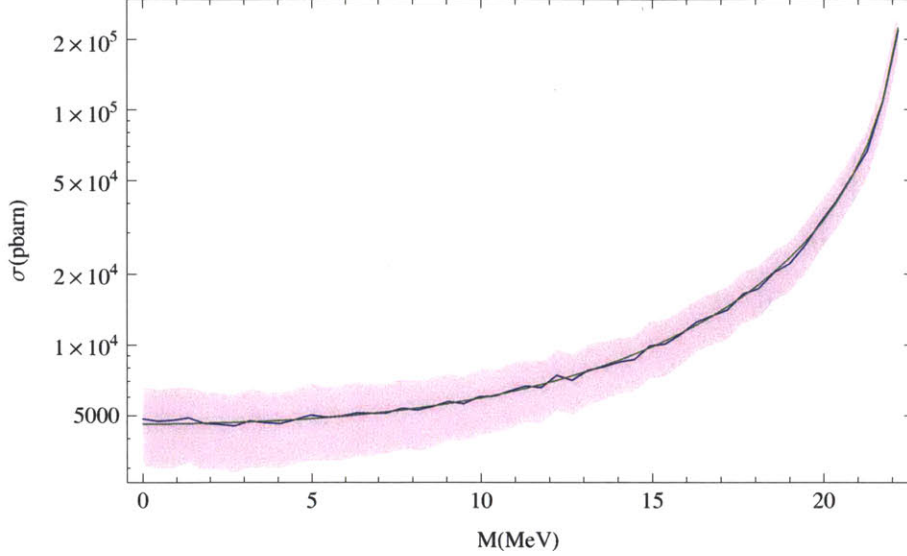
Figure 4-1: Plot of the total unconstrained signal cross section σ (blue curve) as a function of the A' mass M. The number of Monte Carlo events was $\mathcal{N} = 1000$. The pink shaded area is the uncertainty. The analytically integrated cross section is given by the green curve. Note the divergence at $M = E_{CM} = 22.6$ MeV.

taking measurements of the signal process, the requirement that a photon of nonzero energy is detected regulates the singularity by itself. If we impose a cut on E_γ, the cross section will reach zero at some $M^{max} < E_{CM}$, and we do not need to add the loop diagram. As $M \rightarrow E_{CM}$ from below, the maximum photon energy in the CM frame, $E_\gamma = \dfrac{E_{CM}^2 - M^2}{2E_{CM}}$, goes to 0 smoothly, and this factor appears in the phase space. The diminishing phase space dominates the increasing matrix element, so the cross section is zero for $M \geq M^{max}$, and the process is kinematically disallowed.

In Figure 4-2 we present a Monte Carlo computation of the constrained signal cross section as a function of the A' mass. The constraints used are the $2 \rightarrow 2$ analogues of those used for the 3γ background (see Chapter 2 and the following discussion in Section 4.2).

4.2   Background Cross Sections

For the two background processes, we use MadGraph 5 to numerically compute the matrix elements. The information flow for MadGraph 5 consists of the following:
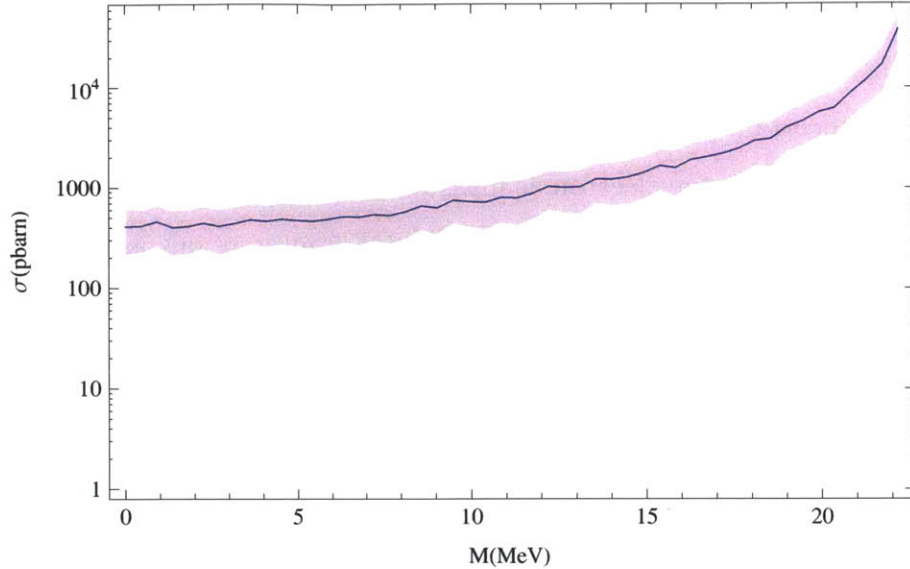
Figure 4-2: Plot of the constrained signal cross section σ as a function of the A' mass M, using the $2 \rightarrow 2$ analogues of the 3γ constraints. The number of Monte Carlo events was $\mathcal{N} = 1000$. The pink shaded area is the uncertainty.

Input: First the desired process is specified. The resulting code takes a table of four-momenta, with one full set $((p_1, p_2, p_3, p_4, p_5)$ for $2 \rightarrow 3$ scattering) of four-momenta for each of $\mathcal{N}$ events.

Output: For each full set of four-momenta, the MadGraph code returns a pair consisting of the set of momenta and the corresponding value of the squared and spin-summed matrix element.

This matrix element is directly inserted for $|\mathcal{M}|^2$ in the differential cross section formula. The generated matrix element code is accessed via a Fortran routine, which reads in many sets of four-momenta, with a placeholder 0 after each set, and to return a file that replaces the 0s by the computed matrix elements. We generate the four-momenta by randomly selecting cascaded $1 \rightarrow 3$ decay parameters in preparation for the Monte Carlo technique described above; the four-momenta are completely specified by these parameters. After running the Fortran routine, we have the center-of-mass parameters and read in the corresponding differential cross sections. This is all the information we need to compute the total cross sections and invariant-mass histograms.

We made a few specifications to optimize the performance of MadGraph. We generated momenta in MeV rather than GeV in order to improve numerical stability, reducing the uncertainty. In addition, MadGraph is designed to be run in the high-energy limit, and treats the electron as massless. We reintroduce the electron mass by a workaround, noting that the τ has the same QED interactions as the electron, but has a different mass. Instead of generating the processes $e^+ + e^- \to 3\gamma$ and $e^+ + e^- \to e^+ + e^- + \gamma$, we generate $\tau^+ + \tau^- \to 3\gamma$ and $\tau^+ + \tau^- \to \tau^+ + \tau^- + \gamma$. MadGraph creates a directory for each process, containing the Fortran code as well as a file called the "parameter card." This file contains the numerical values of Lagrangian parameters for built-in particles. In particular, the mass of the τ is specified. We modify the value of m_τ to match the electron mass, $m_e = 0.511$ MeV. So we have turned the τ into an electron with its mass included in the matrix element computation.

4.3 Results

We computed histograms (Figures 4-3, 4-4) over the full kinematically allowed range of m_{45}, with constraints to regulate the energy singularity for the 3γ process. Specifically, we require each lab energy to be at least 1 MeV. There is still an energy singularity in the e^+ e^- γ process, but it is automatically regulated by kinematic constraints imposed by the detector's measurement, as in the case of the signal cross section. Notice that the 3γ cross section is largest for $m_{45} < 10$ MeV (Figure 4-3), which is in the expected mass range of the A', so we say that the process $e^+ + e^- \to 3\gamma$ can fake an A'.

We imposed constraints by multiplying the differential cross section by a Heaviside Θ function for each constraint. The process $e^+ + e^- \to 3\gamma$ was constrained as per the VEPP-3 setup (lab variables):

50MeV $\leq E_3 \leq$ 400MeV,

$E_4, E_5 \geq 1$ MeV (to cut off an energy singularity),

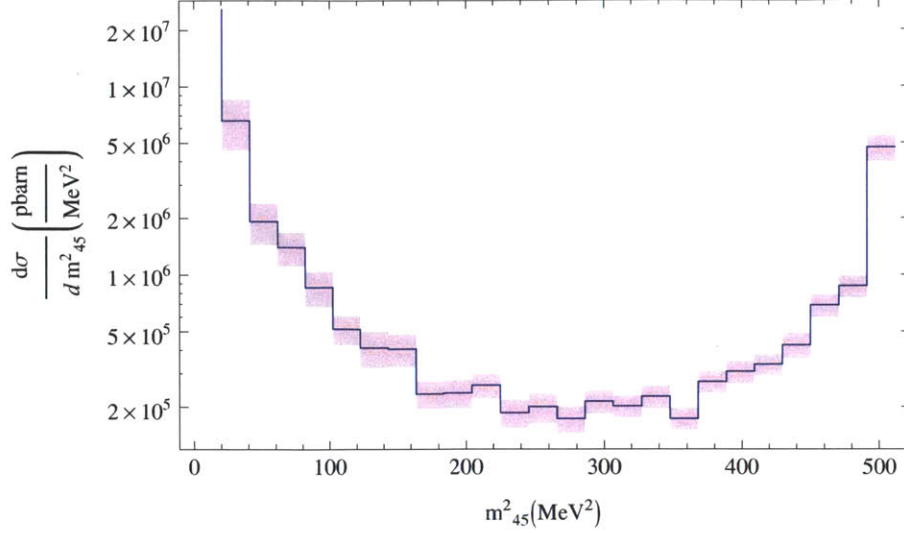$1.5° \leq \theta_3 \leq 4.5°$,

$\theta_4, \theta_5 \notin [1.5°, 4.5°]$.

Figure 4-3: Differential cross section over m_{45}^2, $\dfrac{d\sigma}{dm_{45}^2}$, for $e^+ + e^- \rightarrow 3\gamma$, with the energy singularity regulated. $\mathcal{N} = 5000$ events.

Recall that if two or more photons hit the photometer, we can throw out the event as background. The last constraint ensures that we only consider events in which exactly one photon is detected. The process $e^+ + e^- \rightarrow \gamma + e^+ + e^-$ was constrained as follows:

$50\text{MeV} \leq E_3 \leq 400\text{MeV},$

$1.5° \leq \theta_3, \theta_4 \leq 4.5°.$

For this process, the energy singularity is automatically cut off by the measurement, and there are no identical particles in the final state. Hence, we can physically separate all three final-state particles, allowing the γ to hit the detector and the charged particles to be swept away by a strong magnetic field to the sink. We give the constrained histograms and total cross sections in Figures 4-5, 4-6.

The $e^+\, e^-\, \gamma$ process is suppressed by the positron sink. For Wojtsekhowski's setup, the suppression factor is $\dfrac{1}{50}$. For an ideal detector, the denominator would be infinite, and the positron bremsstrahlung process would be completely suppressed, leaving the 3γ process as the sole background. We will consider a range of suppression factors in our reach plot.
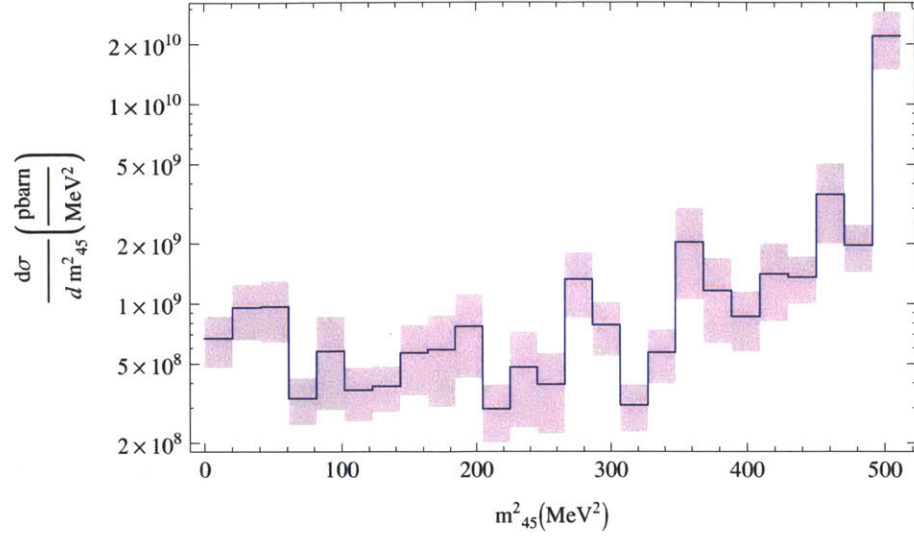
Figure 4-4: Differential cross section over m_{45}^2 for $e^+ + e^- \to \gamma + e^+ + e^-$. The energy singularity is already regulated by the measurement process. $\mathcal{N} = 40000$ events.

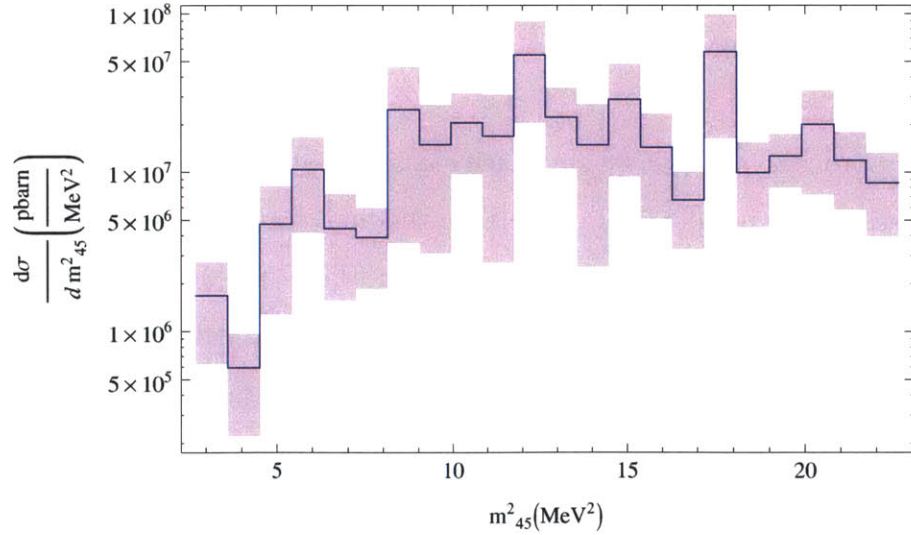

Figure 4-5: Constrained differential cross section over m_{45}^2 for $e^+ + e^- \to 3\gamma$. $\mathcal{N} = 10000$ events.
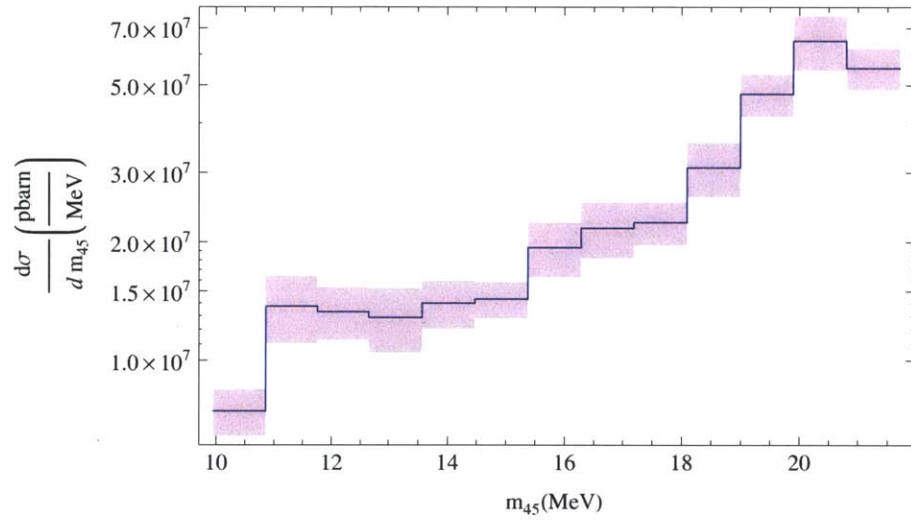
34

Figure 4-6: Constrained differential cross section over m_{45}^2 for $e^+ + e^- \rightarrow \gamma + e^+ + e^-$. $\mathcal{N} = 40000$ events.

Chapter 5

Experimental Reach

A reach plot shows the couplings α' and the A' masses that can be tested at 5σ confidence. It separates $(m_{A'}, \alpha')$ parameter space into two regions, one in which we can claim discovery of an A' gauge boson or exclude such an A', and one in which we cannot. We compute numerical reach plots for the signal process $e^+ + e^- \to \gamma + A'$ over the two backgrounds, 3γ and $e^+e^-\gamma$, relating the A' mass m_A to the coupling constant α'.

In the lab frame, a positron beam impinges upon a stationary electron target, with luminosity $\mathcal{L}$. The number of scattering events of a given process i is $N_i = \mathcal{L}\sigma_i$, where σ_i is the total cross section. In addition, we see in the appendix that the signal cross section is proportional to α'. Hence, if $\sigma_s|_{\alpha'_0}$ is the signal cross section evaluated at a set coupling constant $\alpha'_0 (= 10^{-8})$, then $\sigma_s = \dfrac{\alpha'}{\alpha'_0}\sigma_s|_{\alpha'_0}$ at an arbitrary coupling constant α'. We summarize these results as follows:

$$N_s = \mathcal{L}\sigma_s = \mathcal{L}\frac{\alpha'}{\alpha'_0}\sigma_s|_{\alpha'_0}, \tag{5.1}$$

$$N_b = \mathcal{L}\sigma_b. \tag{5.2}$$

Here, σ_b is the background cross section, with the additional constraint that $m_{45} \in [m'_A - \sigma_{m_{45}}, m'_A + \sigma_{m_{45}}]$. That is, the invariant mass of all of the outgoing particles except one detected photon must be within the experimental mass resolution of the A' mass. Aside from these additional constraints, we impose the exact same kinematic

constraints on both the signal and background processes, treating $p_4 + p_5$ from the background process as we treat the A' momentum q_A in the signal process.

The relation between m'_A and α' comes from imposing 5σ confidence in the cross section measurements, by setting the signal-to-noise ratio to be 5:

$$\frac{N_s}{\sqrt{N_b}} = 5 \qquad \Longrightarrow \qquad \alpha' = 5\sqrt{\frac{\sigma_b}{\mathcal{L}}} \frac{\alpha'_0}{\sigma_s|_{\alpha'_0}}. \tag{5.3}$$

We iterate through values of $m_{A'}$ in the mass range $11 - 22$ MeV and compute the corresponding value of α'. The reach plot is displayed in Figures 5-1. There are two competing effects: the signal matrix element increases due to the soft singularity of QED, while the phase space prefactors in the cross section approach zero. Until $m_{A'}$ gets close to E_{cm}, the increase of $\overline{|\mathcal{M}|^2}$ dominates, so that the reach improves, allowing smaller couplings to be measured. Near the kinematic upper limit, the decreasing phase space is the dominant effect, and the signal cross section approaches zero. This limiting mass is given by $m_{A'} = E_{cm} - E_{3min}$, with the A' emitted at rest and the γ emitted with its minimum experimentally-detectable energy under the VEPP-3 constraints. Near the limiting mass, the reach curve should increase to infinity, preventing the measurement of couplings at the limiting mass. This behavior is not captured under our numerical precision, so we introduce a vertical line by hand at the limiting mass to complete the shape of the reach.

There are additional bounds on the allowed coupling from $(g - 2)$ of the electron and muon. The α' coupling and $m_{A'}$ mass could be measured in a region not already excluded by these bounds. Due to a 3.6 σ discrepancy between the experimental and theoretical values of $(g - 2)_\mu$ [7], the $(g - 2)_\mu$ reach is given by a band in the $(m_{A'}, \alpha')$ plane. With the reach plot given in Figure 5-1, the $(g - 2)$ boundaries are an order of magnitude higher than the reach coupling constant, except for near the kinematic limit. For comparison, we give an alternate reach plot [16], computed using CompHEP[17], a package for the computation of Feynman diagrams, in Figure 5-2. Both reach plots exhibit the same improvement up to the limiting mass, followed by a vertical line. The differences between CompHEP and MadGraph are due to
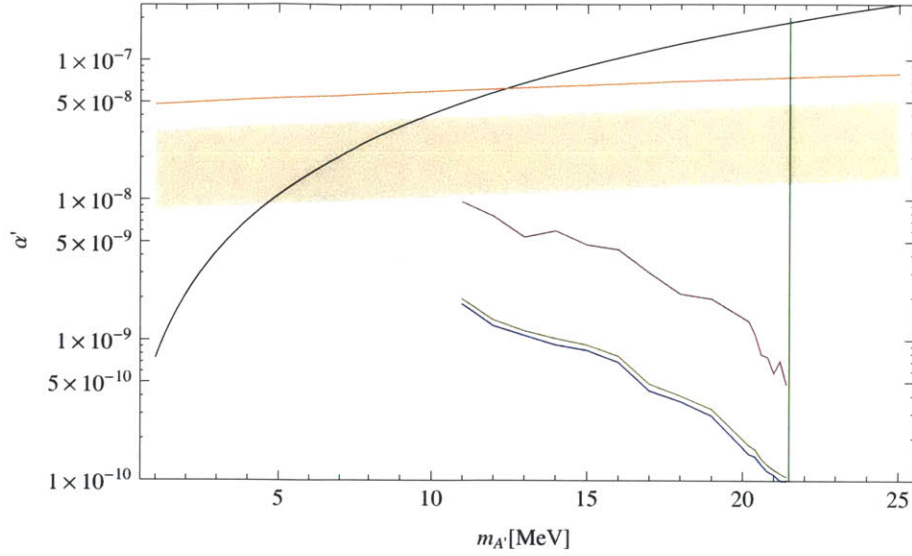
Figure 5-1: Reach plot, with suppression factor $= 1$ (blue), $\dfrac{1}{50}$, (pink), and ∞ (gold). The kinematic upper bound is given by the green vertical line. The shaded region is the $(g-2)_\mu$ band. The orange and black curves are the $(g-2)_\mu$ and $(g-2)_e$ exclusion boundaries, respectively. Any points above these boundaries are forbidden.
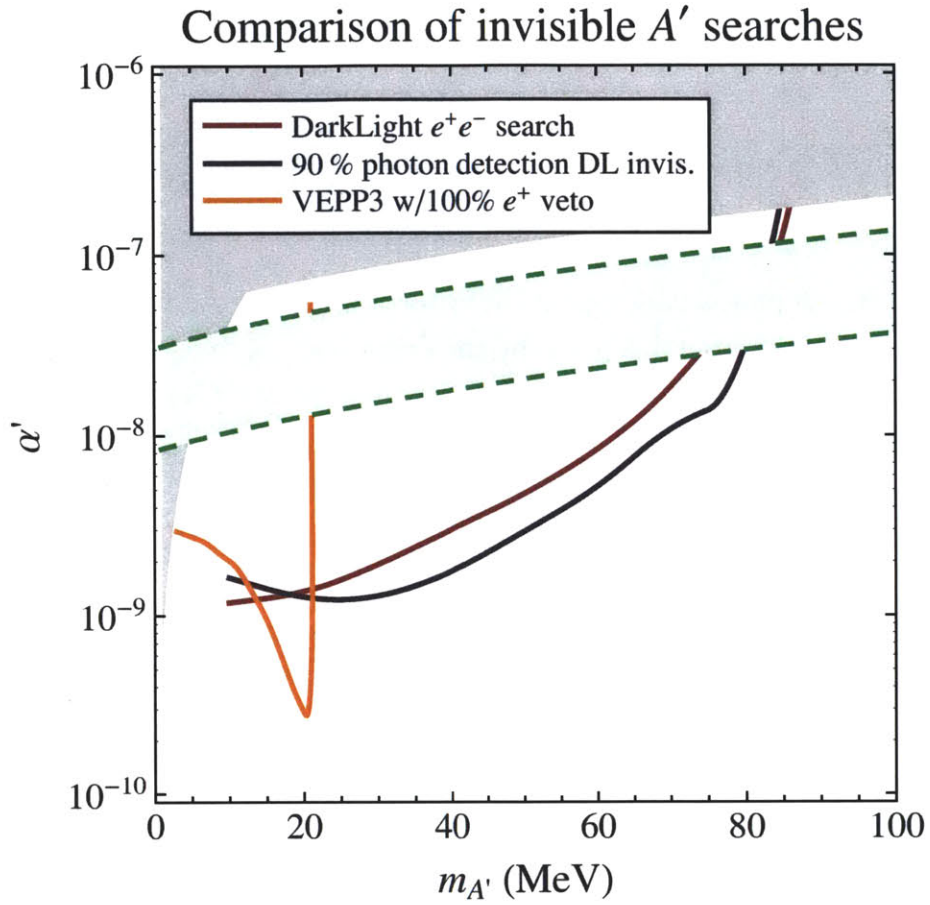
limitations in numerical accuracy.

Figure 5-2: Reach plot computed using CompHEP. The gold curve labelled VEPP-3 is the reach of Wojtsekhowski's setup, with 100% suppression of the $e^+ e^- \gamma$ background. The green shaded region is the $(g-2)_\mu$ band [16].

Chapter 6

Conclusion

In this thesis, we performed an analysis of Wojtsekhowski's VEPP-3 experimental setup for the production of an A' as a product of electron-positron annihilation. Using Monte Carlo integration, we computed total cross-sections under the VEPP-3 constraints for the signal process, $e^+ + e^- \rightarrow \gamma + A'$, and the two dominant background processes, $e^+ + e^- \rightarrow 3\gamma$ and $e^+ + e^- \rightarrow \gamma + e^+ + e^-$. Additionally, we computed composite invariant mass histograms for the two background processes. We found that the 3γ background is dominant, since the alternative background $\gamma\, e^+\, e^-$ is partially suppressed by the positron detector at VEPP-3. In principle, an ideal positron detector would completely eliminate the $\gamma\, e^+\, e^-$ background. Finally, we generated reach plots that display the region of the (m'_A, α') plane for which discovery of the A' can or cannot be claimed.

This analysis is relevant to the DarkLight experiment, and motivates the implementation of invisible A' search in the proposed apparatus. DarkLight uses Rutherford scattering of an e^- beam off of a stationary proton target. The signal process for DarkLight is currently $A' \rightarrow e^+ + e^-$, but with invisible A' search, the signal would be $e^- + p \rightarrow e^- + p + A'$. The dominant background would be $e^- + p \rightarrow e^- + p + 2\gamma$, since we need 2 photons to get a nonzero invariant mass. The Monte Carlo methods we developed are entirely general, and may be directly applied to these processes to generate a reach plot. The DarkLight reach would be comparable to the VEPP-3 reach: VEPP-3 has fewer phase space particles in the final state, so its cross sections

41

are larger. This improves the α' reach for VEPP-3. But the ratio $\dfrac{\sigma_s}{\sqrt{\sigma_b}}$ which occurs in the reach plot is larger for DarkLight than for VEPP-3, since DarkLight could in principle detect and identify all of the final state particles, and DarkLight has a higher instantaneous luminosity. This improves the α' reach for DarkLight, and the improvement may be similar in magnitude to VEPP-3.

Appendix A

Integration of Lorentz-Invariant 3-Body Phase Space

For a $1 \to 2$ decay, the phase space integration gives

$$\int d\Phi_2 = \int \frac{d^4p_1}{(2\pi)^4} \frac{d^4p_2}{(2\pi)^4} (2\pi)^4 \delta^{(4)}(E_{cm} - p_1 - p_2)\theta(E_1)\theta(E_2)(2\pi)^2\delta(p_1^2 - m_1^2)\delta(p_2^2 - m_2^2).$$
(A.1)

Using $p^2 - m^2 = E^2 - (\vec{p}^2 + m^2)$, we have

$$\delta(p^2 - m^2)\theta(E) = \frac{\delta(E - \sqrt{m^2 + |\vec{p}|^2})}{2\sqrt{m^2 + |\vec{p}|^2}}.$$
(A.2)

Hence,

$$
\begin{aligned}
\int d\Phi_2 &= \int \frac{d^3p_1 d^3p_2}{16\pi^2\sqrt{m_1^2 + |\vec{p_1}|^2}\sqrt{m_2^2 + |\vec{p_2}|^2}} \delta^{(4)}(E_{cm} - p_1 - p_2) \\
&= \int \frac{d^3p_1 d^3p_2}{16\pi^2\sqrt{m_1^2 + |\vec{p_1}|^2}\sqrt{m_2^2 + |\vec{p_2}|^2}} \\
&\quad \times \delta(E_{cm} - \sqrt{m_1^2 + |\vec{p_1}|^2} - \sqrt{m_2^2 + |\vec{p_2}|^2})\delta^{(3)}(\vec{p_1} + \vec{p_2}) \\
&= \int d\Omega \int_0^\infty \frac{r^2 dr}{16\pi^2\sqrt{m_1^2 + r^2}\sqrt{m_2^2 + r^2}} \\
&\quad \times \delta(E_{cm} - \sqrt{m_1^2 + r^2} - \sqrt{m_2^2 + r^2}).
\end{aligned}
$$
(A.3)

We make the substitution $u(r) = \sqrt{r^2 + m_1^2} + \sqrt{r^2 + m_2^2}$, so that

$$du = dr \left[\frac{r}{\sqrt{r^2 + m_1^2}} + \frac{r}{\sqrt{r^2 + m_2^2}} \right] = \frac{ur}{\sqrt{r^2 + m_1^2}\sqrt{r^2 + m_2^2}} dr. \qquad (A.4)$$

We change variables in the integration:

$$\int d\Phi_2 = \frac{1}{16\pi^2} \int d\Omega \int_{m_1+m_2}^{\infty} \frac{r(u)}{u} \delta(E_{cm} - u) = \frac{1}{16\pi^2} \int d\Omega \frac{r(u = E_{cm})}{E_{cm}}$$

$$= \frac{1}{32\pi^2} \sqrt{c_1^4 + c_2^4 + 1 - 2c_1^2 c_2^2 - 2c_1^2 - 2c_2^2} \int d\Omega, \qquad (A.5)$$

provided that $E_{cm} > m_1 + m_2$, otherwise $\int d\Phi_2 = 0$. We have written

$$c_1 = \frac{m_1}{E_{cm}}, \qquad c_2 = \frac{m_2}{E_{cm}}. \qquad (A.6)$$

We now decompose $1 \to 3$ decay into $1 \to 2 \to 3$ cascaded decay: 3-body LIPS is given by

$$\int d\Phi_3 = \int \frac{d^4 p_1}{(2\pi)^4} \frac{d^4 p_2}{(2\pi)^4} \frac{d^4 p_3}{(2\pi)^4} (2\pi)^4 \delta^{(4)}(E_{cm} - p_1 - p_2 - p_3)$$

$$\times \theta(E_1)\theta(E_2)\theta(E_3)(2\pi)^3 \delta(p_1^2 - m_1^2)\delta(p_2^2 - m_2^2)\delta(p_3^2 - m_3^2). \ (A.7)$$

We introduce an intermediate mass Q, so that $E_{cm} \to p_1 + Q$ and $Q \to p_2 + p_3$. We integrate over its momentum $d^4 p_q$, and over Q^2 subject to the constraints

$$Q^2 = p_q^2 = (E_{cm} - p_1)^2 = E_{cm}^2 + m_1^2 - 2E_{cm}E_1$$

$$\leq E_{cm}^2 + m_1^2 - 2E_{cm}m_1$$

$$= (E_{cm} - m_1)^2 \qquad (A.8)$$

and

$$Q^2 = (p_2 + p_3)^2 = m_2^2 + m_3^2 + 2p_2 \cdot p_3. \qquad (A.9)$$

44

Moving to the center of momentum frame of p_2 and p_3, $\vec{p}_2 = -\vec{p}_3$. In this frame,

$$Q^2 = m_2^2 + m_3^2 + 2E_2E_3 + 2\vec{p}_2^2. \tag{A.10}$$

With $E_2E_3 = \sqrt{\vec{p}_2^2 + m_2^2} \cdot \sqrt{\vec{p}_2^2 + m_3^2}$, we see that this is minimized for $\vec{p}_2 = 0$, that is, $Q^2 \geq (m_2 + m_3)^2$. Under this integration, we make the substitution $\delta^{(4)}(E_{cm} - p_1 - p_2 - p_3) \mapsto (2\pi)^4\delta^{(4)}(E_{cm} - p_1 - p_q)\delta^{(4)}(p_q - p_2 - p_3)$ and include the factors $\delta(p_q^2 - Q^2)$ (p_q on mass shell) and $\theta(E_q)$. This second factor does not change the integral because E_{cm}, p_1, p_2, p_3 are all timelike momenta with positive energy, so p_q must be as well. We obtain

$$
\begin{aligned}
\int d\Phi_3 &= \frac{1}{2\pi} \int_{(m_2+m_3)^2}^{(E_{cm}-m_1)^2} dQ^2 \int \frac{d^4p_1}{(2\pi)^4} \frac{d^4p_q}{(2\pi)^4} (2\pi)^6 \delta^{(4)}(E_{cm} - p_1 - p_q)\theta(E_1)\theta(E_p) \\
&\quad \times \delta(p_1^2 - m_1^2)\delta(p_q^2 - Q^2) \\
&\quad \times \int \frac{d^4p_2}{(2\pi)^4} \frac{d^4p_3}{(2\pi)^4} (2\pi)^6 \delta^{(4)}(p_q - p_2 - p_3)\theta(E_2)\theta(E_3) \\
&\quad \times \delta(p_2^2 - m_2^2)\delta(p_3^2 - m_3^2) \\
&= \frac{1}{2\pi} \int_{(m_2+m_3)^2}^{(E_{cm}-m_1)^2} dQ^2 \int d\Phi_2(E_{cm} \to p_1 + p_q) \int d\Phi_2(p_q \to p_2 + p_3) \\
&= \frac{1}{(2\pi)(32\pi^2)^2} \int_{(m_2+m_3)^2}^{(E_{cm}-m_1)^2} dQ^2 \left[\sqrt{c_1^4 + c_q^4 + 1 - 2c_1^2c_q^2 - 2c_1^2 - 2c_q^2} \right. \\
&\quad \left. \times \sqrt{\left(\frac{c_2}{c_q}\right)^4 + \left(\frac{c_3}{c_q}\right)^4 + 1 - 2\left(\frac{c_2}{c_q} \cdot \frac{c_3}{c_q}\right)^2 - 2\left(\frac{c_2}{c_q}\right)^2 - 2\left(\frac{c_3}{c_q}\right)^2} \right] \\
&\quad \times d\Omega_{1q}d\Omega_{23}, \tag{A.11}
\end{aligned}
$$

where $c_q = \dfrac{Q}{E_{cm}}$ and $c_i = \dfrac{m_i}{E_{cm}}$, $i = 1, 2, 3$.

For the case $c_1 = c = \dfrac{m}{E_{cm}}$, $c_2 = c_3 = 0$, we obtain (changing variables to c_q)

$$\int d\Phi_3 = \frac{E_{cm}^2}{(2\pi)(32\pi^2)^2} \int_0^{(1-c)^2} d(c_q^2)\sqrt{c^4 + c_q^4 + 1 - 2c^2c_q^2 - 2c_1^2 - 2c_q^2}d\Omega_{1q}d\Omega_{23}. \tag{A.12}$$

45

Evaluating this dimensionless integral, we obtain

$$d\Phi_3 = \frac{E_{cm}^2}{(4\pi) \cdot (32\pi^2)^2}(1 - c^4 + 4c^2 \ln c)d\Omega_{1q}d\Omega_{23}. \tag{A.13}$$

For the case $c_2 = c$, $c_1 = c_3 = 0$, we have

$$\begin{aligned}
d\Phi_3 &= \frac{E_{cm}^2}{(2\pi) \cdot (32\pi^2)^2}\int_{c^2}^1 d(c_q^2)\sqrt{c_q^4 + 1 - 2c_q^2}\sqrt{\left(\frac{c}{c_q}\right)^4 + 1 - 2\left(\frac{c}{c_q}\right)^2}d\Omega_{1q}d\Omega_{23} \\
&= \frac{E_{cm}^2}{(4\pi) \cdot (8\pi)^2}(1 - c^4 + 4c^2 \ln c)d\Omega_{1q}d\Omega_{23}. \tag{A.14}
\end{aligned}$$

Since the Q is a fictional particle we have used to arbitrarily group two of the three masses, the result should be independent of our choice of the nonzero mass. We see that this is indeed the case.

Appendix B

Calculation of the $e^+ + e^- \to \gamma + A'$ Matrix Element

To calculate the signal process, we use the standard QED Lagrangian with the additional interaction $-g A'_\mu \bar{\psi} \gamma^\mu \psi$ and a mass term $m^2_{A'} A'_\mu A'^\mu$. This gives

$$
\begin{aligned}
i\mathcal{M} \;=\; \bar{v}(p_+) & \left[(-ig\gamma^\mu) \epsilon^*_\mu(q_A) \frac{i(\slashed{p}_- - \slashed{q}_\gamma + m)}{(p_- - q_\gamma)^2 - m^2} (-ie\gamma^\nu) \epsilon^*_\nu(q_\gamma) \right. \\
& \left. + (-ie\gamma^\mu) \epsilon^*_\mu(q_\gamma) \frac{i(\slashed{q}_\gamma - \slashed{p}_+ + m)}{(p_+ - q_\gamma)^2 - m^2} (-ig\gamma^\nu) \epsilon^*_\nu(q_A) \right] u(p_-). \quad \text{(B.1)}
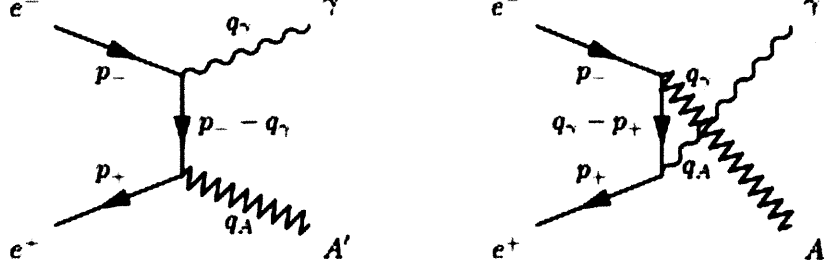\end{aligned}
$$

Figure B-1: Tree-level diagrams for the annihilation of an electron and positron to an A' and a photon. Note the close analogy with the $e^+ + e^- \to 2\gamma$ process from standard quantum electrodynamics.

We sum over final spins and average over initial spins, and obtain

$$
\begin{aligned}
\overline{|\mathcal{M}|^2} &= \frac{1}{4}\sum_{spins}|\mathcal{M}|^2 = \frac{g^2 e^2}{4}\sum_{s,s'} \epsilon_\mu^{s*}(q_\gamma)\epsilon_\lambda^s(q_\gamma)\epsilon_\nu^{s'*}(q_A)\epsilon_\sigma^{s'}(q_A) \\
&\quad \times \mathrm{tr}\left[(\not{p}_- + m)\left(\gamma^\lambda\frac{\not{p}_- - \not{q}_\gamma + m}{(p_- - q_\gamma)^2 - m^2}\gamma^\sigma - \gamma^\sigma\frac{\not{p}_+ - \not{q}_\gamma - m}{(p_+ - q_\gamma)^2 - m^2}\gamma^\lambda\right)\right. \\
&\quad \left. \times (\not{p}_+ - m)\left(\gamma^\nu\frac{\not{p}_- - \not{q}_\gamma + m}{(p_- - q_\gamma)^2 - m^2}\gamma^\mu - \gamma^\mu\frac{\not{p}_+ - \not{q}_\gamma - m}{(p_+ - q_\gamma)^2 - m^2}\gamma^\nu\right)\right] \quad (B.2) \\
&= \frac{g^2 e^2}{4}\left[\frac{1}{(2p_- \cdot q_\gamma)^2}\mathrm{tr}[(\not{p}_- + m)\gamma_\mu(\not{p}_- - \not{q}_\gamma + m)\gamma_\nu\right. \\
&\qquad\qquad\qquad\qquad \times (\not{p}_+ - m)\gamma^\nu(\not{p}_- - \not{q}_\gamma + m)\gamma^\mu] \\
&\quad - \frac{1}{4p_- \cdot q_\gamma p_+ \cdot q_\gamma}\mathrm{tr}[(\not{p}_- + m)\gamma_\mu(\not{p}_- - \not{q}_\gamma + m)\gamma_\nu \\
&\qquad\qquad\qquad\qquad \times (\not{p}_+ - m)\gamma^\mu(\not{p}_+ - \not{q}_\gamma - m)\gamma^\nu] \\
&\quad - \frac{1}{4p_- \cdot q_\gamma p_+ \cdot q_\gamma}\mathrm{tr}[(\not{p}_- + m)\gamma_\nu(\not{p}_+ - \not{q}_\gamma - m)\gamma_\mu \\
&\qquad\qquad\qquad\qquad \times (\not{p}_+ - m)\gamma^\nu(\not{p}_- - \not{q}_\gamma + m)\gamma^\mu] \\
&\quad + \frac{1}{(2p_+ \cdot q_\gamma)^2}\mathrm{tr}[(\not{p}_- + m)\gamma_\nu(\not{p}_+ - \not{q}_\gamma - m)\gamma_\mu \\
&\qquad\qquad\qquad\qquad \left. \times (\not{p}_+ - m)\gamma^\mu(\not{p}_+ - \not{q}_\gamma - m)\gamma^\nu]\right].
\end{aligned}
$$

$$(B.3)$$

We have used $(\bar{u}\gamma_\mu\gamma_\nu\gamma_\lambda v)^\dagger = v^\dagger\gamma_\lambda^\dagger\gamma_\nu^\dagger\gamma_\mu^\dagger\gamma_0 u = \bar{v}\gamma_\lambda\gamma_\nu\gamma_\mu u$, and replaced $\sum_s \epsilon_\mu^{s*}(p)\epsilon_\lambda^s(p) \to -\eta_{\mu\lambda}$.

Labeling these traces by I, II, III, and IV, note that, up to cyclic ordering, III is II

48

with all of the factors of the trace reversed; equation (A.28) in [3] implies that II = III. The fourth trace may be dealt with by noting that an even number of m factors must be selected in each nonzero term. So we can multiply each m by -1 without changing the result. Reversing the resulting trace, we see that IV = I$(p_- \leftrightarrow p_+)$ = I$(t \leftrightarrow u)$.

$$
\begin{aligned}
I &= \mathrm{tr}[(\not{p}_- + m)\gamma_\mu(\not{p}_- - \not{q}_\gamma + m)\gamma_\nu(\not{p}_+ - m)\gamma^\nu(\not{p}_- - \not{q}_\gamma + m)\gamma^\mu] \\
&= -2\mathrm{tr}[(\not{p}_- + m)\gamma_\mu(\not{p}_- - \not{q}_\gamma + m)(\not{p}_+ + 2m)(\not{p}_- - \not{q}_\gamma + m)\gamma^\mu] \\
&= 4\mathrm{tr}[(\not{p}_- - 2m)(\not{p}_- - \not{q}_\gamma + m)(\not{p}_+ + 2m)(\not{p}_- - \not{q}_\gamma + m)] \\
&= 4\{4[2(p_- \cdot (p_- - q_\gamma))(p_+ \cdot (p_- - q_\gamma)) - (p_- \cdot p_+)(p_- - q_\gamma)^2] + 8m^2 p_- \cdot (p_- - q_\gamma) \\
&\quad + 4m^2 p_- \cdot p_+ + 8m^2 p_- \cdot (p_- - q_\gamma) - 8m^2 p_+ \cdot (p_- - q_\gamma) - 16m^2(p_- - q_\gamma)^2 \\
&\quad - 8m^2 p_+ \cdot (p_- - q_\gamma) - 16m^4\} \\
&= 16[2(p_- \cdot (p_- - q_\gamma))(p_+ \cdot (p_- - q_\gamma)) - (p_- \cdot p_+)(p_- - q_\gamma)^2 + 4m^2 p_- \cdot (p_- - q_\gamma) \\
&\quad + m^2 p_- \cdot p_+ - 4m^2 p_+ \cdot (p_- - q_\gamma) - 4m^2(p_- - q_\gamma)^2 - 4m^4]. \quad (\text{B.4})
\end{aligned}
$$

We introduce Mandlestam variables:

$$
s = (p_+ + p_-)^2 \Rightarrow p_+ \cdot p_- = \frac{s}{2} - m^2, \tag{B.5}
$$

$$
t = (p_- - q_\gamma)^2 \Rightarrow p_- \cdot q_\gamma = \frac{1}{2}(m^2 - t), \tag{B.6}
$$

$$
u = (p_+ - q_\gamma)^2 \Rightarrow p_+ \cdot q_\gamma = \frac{1}{2}(m^2 - u), \tag{B.7}
$$

$$
s + t + u = M^2 + 2m^2, \tag{B.8}
$$

where m is the electron mass and M is the A' mass. We have

$$
p_- \cdot (p_- - q_\gamma) = m^2 - \frac{1}{2}(m^2 - t) = \frac{1}{2}(m^2 + t), \tag{B.9}
$$

$$
p_+ \cdot (p_- - q_\gamma) = \frac{s}{2} - m^2 - \frac{1}{2}(m^2 - u) = \frac{1}{2}(s + u - 3m^2). \tag{B.10}
$$

So

$$
\begin{aligned}
I &= 16\left[\frac{1}{2}(m^2+t)(s+u-3m^2) - \left(\frac{s}{2}-m^2\right)t + 2m^2(m^2+t) + m^2\left(\frac{s}{2}-m^2\right)\right.\\
&\quad \left.-2m^2(s+u-3m^2) - 4m^2t - 4m^4\right]\\
&= 16\left[\frac{st}{2} + \frac{tu}{2} - \frac{st}{2} + m^2\left(\frac{s}{2} + \frac{u}{2} - \frac{3}{2}t + t + 2t + \frac{s}{2} - 2s - 2u - 4t\right)\right.\\
&\quad \left.+m^4\left(-\frac{3}{2} + 2 - 1 + 6 - 4\right)\right],
\end{aligned}
$$

(B.11)

so that

$$
I = 8[tu - m^2(2s + 5t + 3u) + 3m^4].
$$

(B.12)

It immediately follows that

$$
IV = 8[tu - m^2(2s + 5u + 3t) + 3m^4].
$$

(B.13)

The remaining trace is computed analogously, and yields

$$
\begin{aligned}
II &= \mathrm{tr}[(\slashed{p}_- + m)\gamma_\mu(\slashed{p}_- - \slashed{q}_\gamma + m)\gamma_\nu(\slashed{p}_+ - m)\gamma^\mu(\slashed{p}_+ - \slashed{q}_\gamma - m)\gamma^\nu]\\
&= 16[-2((p_- - q_\gamma)\cdot(p_+ - q_\gamma))(p_+\cdot p_-) - m^2 p_+\cdot(p_- - q_\gamma) + m^2(p_+ - p_-)^2\\
&\quad -m^2 p_-\cdot(p_+ - q_\gamma) - 2m^4],
\end{aligned}
$$

(B.14)

where we have made use of equation (A.29) in [3] multiple times. We insert Mandlestam variables as follows:

$$
\begin{aligned}
(p_- - q_\gamma)\cdot(p_+ - q_\gamma) &= \frac{s}{2} - m^2 - \frac{1}{2}(m^2 - u) - \frac{1}{2}(m^2 - t) + q_\gamma^2 = \frac{s+t+u}{2} - 2m^2\\
&= \frac{M^2}{2} - m^2,
\end{aligned}
$$

(B.15)

$$
p_-\cdot(p_+ - q_\gamma) = \frac{s}{2} - m^2 - \frac{1}{2}(m^2 - t) = \frac{1}{2}(s + t - 3m^2),
$$

(B.16)

$$
(p_+ - p_-)^2 = 2m^2 - 2p_+\cdot p_- = 2m^2 - 2\left(\frac{s}{2} - m^2\right) = 4m^2 - s.
$$

(B.17)

Hence

$$
\begin{aligned}
\mathrm{II} \;=\; & 16\left[-(M^2-2m^2)\left(\frac{s}{2}-m^2\right)-\frac{m^2}{2}(s+u-3m^2)\right. \\
& \left.+m^2(4m^2-s)-\frac{m^2}{2}(s+t-3m^2)-2m^4\right] \\
=\; & 8[-M^2s+m^2(2M^2+2s-s-u-2s-s-t)+m^4(-4+3+4+3-2)] \\
=\; & 8[-M^2s+m^2(M^2-s)+2m^4] \tag{B.18} \\
=\; & \mathrm{III}. \tag{B.19}
\end{aligned}
$$

The exact result is given by

$$
\overline{|\mathcal{M}|^2}=\frac{g^2e^2}{4}\left[\frac{\mathrm{I}}{4(p_-\cdot q_\gamma)^2}-\frac{\mathrm{II}}{2(p_-\cdot q_\gamma)(p_+\cdot q_\gamma)}+\frac{\mathrm{IV}}{4(p_+\cdot q_\gamma)^2}\right]. \tag{B.20}
$$

If we applied the approximation $m^2\ll s,t,u,M^2$, we would obtain

$$
\overline{|\mathcal{M}|^2}\approx 2g^2e^2\left[\frac{u}{t}+\frac{2M^2s}{tu}+\frac{t}{u}\right]. \tag{B.21}
$$

But since we compute the phase space integrals by numerical Monte Carlo techniques, there is no need to make such an approximation. We use the exact matrix element.

The differential cross-section is given by equation (6.47) in [14]:

$$
\frac{d\sigma}{d\theta_{CM}}=\frac{1}{32\pi E_{CM}^2}\cdot\frac{E_\gamma}{|\vec{p}_+|}\overline{|\mathcal{M}|^2}, \tag{B.22}
$$

where $E_\gamma=\dfrac{E_{CM}^2-M^2}{2E_{CM}}$ is the center-of-mass energy of the outgoing photon, and $|\vec{p}_+|=\sqrt{\dfrac{E_{CM}^2}{4}-m^2}$ is the momentum of each incoming particle. The factor of $E_{CM}^2-M^2$ in the numerator enforces the kinematic condition $M<E_{CM}$. Note that the cross-section is not Lorentz invariant, but it is invariant under boosts in the 3 direction. So we could have computed $\dfrac{|\vec{q}_\gamma|}{|\vec{p}_+|}$ in either the lab or CM frames: it is most convenient to use the CM frame, as we have done.

Bibliography

[1] **WMAP** Collaboration, E. Komatsu et al., Five-Year Wilkinson Microwave Anisotropy Probe (WMAP) Observations: Cosmological Interpretation, Astrophys. J. Suppl. 180 (2009) 330-376, [arXiv:0803.0547].

[2] E. A. Baltz, J. Edsjo, K. Freese, and P. Gondolo. *The cosmic ray positron excess and neutralino dark matter.* **Phys. Rev. D 65**, 063511-063520 (2002) [arXiv:astro-ph/0109318v2]

[3] M.E. Peskin and D.V. Schroeder. *An Introduction to Quantum Field Theory.* USA: Addison-Wesley (1995) 842 p.

[4] N. Arkani-Hamed, D. P. Finkbeiner, T. R. Slatyer, and N. Weiner, *A Theory of Dark Matter*, Phys. Rev. **D79** (2009) 015014, [arXiv:0810.0713].

[5] Y. Nomura and J. Thaler, *Dark Matter through the Axion Portal*, [arXiv:0810.5397].

[6] PAMELA Collaboration, O. Adriani et al., *An anomalous positron abundance in cosmic rays with energies 1.5-100 GeV*, **Nature 458** (2009) 607-609, [arXiv:0810.4995].

[7] M. Davier, A. Hoecker, B. Malaescu, C.Z. Yuan, and Z. Zhang. *Reevaluation of the hadronic contribution to the muon magnetic anomaly using new $e^+e^- \rightarrow \pi^+\pi^-$ cross section data from BABAR*, **Eur. Phys. J. C. 66** (2010) 1-9, [arXiv:0908.4300v2].

[8] C. Boehm and P. Fayet, *Scalar dark matter candidates*, Nucl. Phys. **B683** (2004) 219

[9] D. Nikolenko, I. Rachek, and B. Wojtsekhowski. *Searching for a new force at VEPP-3.*

[10] M. Freytsis, G. Ovanesyan, J. Thaler. *Dark Force Detection in Low Energy e-p Collisions*, [arXiv:0909.2862v2]

[11] DarkLight Collaboration, P. Balakrishnan et al., *A Proposal for the DarkLight Experiment at the Jefferson Laboratory Free Electron Laser.* (Dec. 1, 2010).

[12] University of Illinois: Urbana-Champaign, High Energy Physics group. *MadGraph 5.* madgraph.hep.uiuc.edu/

[13] P.R. Bevington and D.K. Robinson. *Data reduction and analysis for the physical sciences.* USA: McGraw-Hill (2003) 320 p.

[14] D.J. Griffiths. *Introduction to Elementary Particles.* USA: Wiley-VCH (2008) 454 p.

[15] G. Cowan. *Monte Carlo Techniques.* Lawrence-Berkeley National Laboratory. **The Review of Particle Physics**, *34.* (2011)

[16] Yonatan Kahn, private communication.

[17] CompHEP Collaboration. E.Boos, V.Bunichev, M.Dubinin, L.Dudko, V.Edneral, V.Ilyin, A.Kryukov, V.Savrin, A. Semenov, A. Sherstnev. CompHEP: a package for evaluation of Feynman diagrams, integration over multi-particle phase space and event generation. http://comphep.sinp.msu.ru/.